

# Development and Initial Test Results of the In-Situ Characterization of Irradiated Materials under Deformation



Maxim Gussev  
Philip Edmondson  
Brian Eckhart  
Keith Leonard

**February 2017**

**Approved for public release.  
Distribution is unlimited.**

## DOCUMENT AVAILABILITY

Reports produced after January 1, 1996, are generally available free via US Department of Energy (DOE) SciTech Connect.

**Website** <http://www.osti.gov/scitech/>

Reports produced before January 1, 1996, may be purchased by members of the public from the following source:

National Technical Information Service  
5285 Port Royal Road  
Springfield, VA 22161  
**Telephone** 703-605-6000 (1-800-553-6847)  
**TDD** 703-487-4639  
**Fax** 703-605-6900  
**E-mail** [info@ntis.gov](mailto:info@ntis.gov)  
**Website** <http://classic.ntis.gov/>

Reports are available to DOE employees, DOE contractors, Energy Technology Data Exchange representatives, and International Nuclear Information System representatives from the following source:

Office of Scientific and Technical Information  
PO Box 62  
Oak Ridge, TN 37831  
**Telephone** 865-576-8401  
**Fax** 865-576-5728  
**E-mail** [reports@osti.gov](mailto:reports@osti.gov)  
**Website** <http://www.osti.gov/contact.html>

This report was prepared as an account of work sponsored by an agency of the United States Government. Neither the United States Government nor any agency thereof, nor any of their employees, makes any warranty, express or implied, or assumes any legal liability or responsibility for the accuracy, completeness, or usefulness of any information, apparatus, product, or process disclosed, or represents that its use would not infringe privately owned rights. Reference herein to any specific commercial product, process, or service by trade name, trademark, manufacturer, or otherwise, does not necessarily constitute or imply its endorsement, recommendation, or favoring by the United States Government or any agency thereof. The views and opinions of authors expressed herein do not necessarily state or reflect those of the United States Government or any agency thereof.

**ORNL/TM-2017/111**  
**M3LW-17OR0402025**

Fusion and Materials for Nuclear Systems Division  
Materials Science and Technology Division

**DEVELOPMENT AND INITIAL TEST RESULTS OF THE IN-SITU  
CHARACTERIZATION OF IRRADIATED MATERIALS UNDER  
DEFORMATION**

Maxim Gussev  
Philip Edmondson  
Brian Eckhart  
Keith J. Leonard

Date Published: February 2017

Prepared under the direction of the  
U.S. Department of Energy  
Office of Nuclear Energy  
Light Water Reactor Sustainability Program  
Materials Aging and Degradation Pathway

Prepared by  
OAK RIDGE NATIONAL LABORATORY  
Oak Ridge, TN 37831-6285  
managed by  
UT-BATTELLE, LLC  
for the  
U.S. DEPARTMENT OF ENERGY  
under contract DE-AC05-00OR22725



## CONTENTS

LIST OF FIGURES .....	v
LIST OF TABLES .....	v
ABBREVIATED TERMS .....	vii
EXECUTIVE SUMMARY .....	ix
1. INTRODUCTION. MOTIVATION FOR IMPLEMENTING IN-SITU TESTING .....	1
2. VERSA 3D SEM: GENERAL DESCRIPTION AND SYSTEM PARAMETERS .....	2
3. MINIATURE TENSILE STAGE FOR IN-SITU TESTING .....	3
4. SPECIMEN DESIGN AND PRODUCTION .....	5
4.1 AVAILABLE IRRADIATED MATERIALS .....	5
4.2 SPECIMEN GEOMETRY .....	5
4.3 SPECIMEN FABRICATION APPROACH .....	6
5. PRELIMINARY RESULTS OF THE IN SITU TESTS .....	8
5.1 INTRODUCTION .....	8
5.2 TESTED MATERIAL .....	8
5.3 MECHANICAL BEHAVIOR .....	9
5.4 IN-SITU TEST AND SURFACE TOPOLOGY EVOLUTION .....	9
5.5 ANALYSIS OF THE EBSD MAPS TAKEN DURING THE IN-SITU TEST .....	12
5.6 EBSD IMAGE QUALITY EVOLUTION .....	14
5.7 EBSD STRAIN METRIC ANALYSIS .....	15
5.8 STRAIN-INDUCED PHENOMENA IN AUSTENITIC STAINLESS STEEL .....	17
6. SUMMARY AND CONCLUSIONS .....	19
7. ACKNOWLEDGMENTS .....	20
8. REFERENCES .....	20



## LIST OF FIGURES

Figure 1. General view of the VERSA 3D dual beam (scanning electron microscope and ion beam). .....	2
Figure 2. Left: General view of the tensile stage (Kammrath and Weiss Technologies, Inc., Model MZ.Sb). .....	4
Figure 3. General view of the heater (left) and the enlarged view of the heating element (right).....	4
Figure 4. Tensile stage control modules located on the cart.....	5
Figure 5. Geometry and dimensions of the ultra-miniature specimen for in-situ testing. ....	6
Figure 6. Sherline CNC milling machine, model 2010 (at the left) and specimen manufacturing steps (at the right). Images of the machining are slightly blurry because this process is performed in a water-filled container. ....	7
Figure 7. A 718-alloy miniature specimen (left), a 3D-image of typical tool marks on the specimen edge (top right), and miniature specimens mounted in epoxy (bottom right). ....	7
Figure 8. The representative tensile curve for the SW'-alloy (annealed nuclear-grade 304L steel). ....	9
Figure 9. EBSD IFP and image quality (IQ) maps for the reference area prior to deformation.....	10
Figure 10. The tensile curve from the in-situ test (thick red line) compared to results from the ordinary tensile test (thin blue line). ....	10
Figure 11. SEM images taken at different strain levels. ....	12
Figure 12. Evolution of the IPF (colored in the tensile direction), IQ, GROD, and kernel average misorientation (KAM) maps for the same area at different strain levels.....	13
Figure 13. Degradation of the EBSD data at large strains compared to the reference image (Step 0). ....	14
Figure 14. EBSD data quality (fraction of “good points”) as a function of local strain level. ....	15
Figure 15. GROD as a function of the strain level. ....	16
Figure 16. Evolution of the KAM parameter as a function of the local strain level.....	16
Figure 17. Deformation twin appearance and evolution with strain increase.....	18
Figure 18. EBSD data for the area shown above. ....	18
Figure 19. An example of grain rotation behavior.....	19

## LIST OF TABLES

Table 1. Composition and condition of material investigated .....	9
Table 2. Mechanical properties of the SW'-alloy.....	9



## ABBREVIATED TERMS

BSE	back scatter electron detector
CAD	computer-aided design
CERT	constant extension rate test
CIR	Cooperative IASCC Research program
CNC	computer numeric control
dpa	displacement per atom
EBSD	electron back scatter diffraction
EDS	energy dispersive x-ray spectroscopy
EDT	electron detector
FEG	field emission gun
FIB-STEM	focused ion beam scanning electron microscope/microscopy
GROD	grain reference orientation deviation
HR-EBSD	high-resolution electron back scatter diffraction
IASCC	irradiation-assisted stress corrosion cracking
IPF	inverse pole figure
IQ	image quality
KAM	kernel average misorientation
LAMDA	Low Activation Materials Development and Analysis
LWR	light-water reactor
LWRS	Light-Water Reactor Sustainability Program
NRTL	Nationally Recognized Testing Laboratory
ORNL	Oak Ridge National Laboratory
SEM	scanning electron microscope/microscopy
STEM	scanning transmission electron microscopy



## EXECUTIVE SUMMARY

This report describes the development and implementation of the in-situ mechanical test method at Oak Ridge National Laboratory's Low Activation Materials Development and Analysis (LAMDA) facility and provides some preliminary results obtained using non-irradiated, high-purity, nuclear-grade 304L steel. The report is divided into chapters that describe each of the different aspects related to the in-situ testing. Chapter 1 reviews the background, motivation, and advantages of the in-situ mechanical testing and describes some recent literature results obtained on the non-irradiated materials. This chapter also highlights existing knowledge gaps and provides motivation for investigating plastic strain mechanisms in irradiated steels and alloys. Chapter 2 describes an advanced modern scanning electron microscope (VERSA 3D) available at the LAMDA facility. Its parameters and the tools available for analysis are described in detail. Chapter 3 discusses criteria used for selection of a particular tensile stage model and describes the selected model in detail. Chapter 4 provides a brief overview of the available irradiated materials and offers an approach for production of miniature irradiated tensile specimens. Specimen production at LAMDA may reduce the cost of acquiring new irradiated materials and will allow for the more efficient use of the available sample inventory. Finally, Chapter 5 demonstrates some results obtained during the in-situ tensile testing and describes the advantages of the described testing scheme. The conclusion summarizes the work performed and briefly discusses the future activity.



## 1. INTRODUCTION. MOTIVATION FOR IMPLEMENTING IN-SITU TESTING

Materials in nuclear power plants are exposed to a harsh environment that combines stress, temperature, and radiation fields coupled with transmutation effects. All of these factors stimulate multiple degradation modes, including radiation hardening and embrittlement, radiation-induced segregation, swelling, and helium and hydrogen accumulation, just to name a few. Because of intensive research in the area of radiation-induced material degradation and the development of new materials, some damage modes have been successfully mitigated or are, at the very least, understood well enough to be controlled.

Nevertheless, several negative phenomena continue to influence the performance of in-reactor materials. For example, irradiation-assisted stress corrosion cracking (IASCC) is recognized as a critical concern associated with austenitic steels (e.g., 304L and 316L) which are widely used in the light-water reactors (LWR) operating environments [1, 2, 3]. Even though several new materials have come into use, the 300-series steels are expected to remain in service for at least the next 20–30 years, if not longer. As the existing fleet of LWRs ages, the IASCC-related issues are expected to become more severe. Consequently, this aspect is under active investigation by the Light-Water Reactor Susceptibility (LWRS) program.

IASCC is a complex process involving many contributing factors, including microstructural and microchemical changes induced by irradiation [1]. At a high-damage dose (20–40 displacements per atom [dpa]), stress corrosion cracking in 300-series steels may occur even in a low-potential corrosion environment—where a very low crack-growth rate was observed in non-irradiated or low-dose irradiated materials [4]. Recently, a close connection between plastic-strain localization (dislocation channeling) and IASCC susceptibility was recognized [1, 2], with dislocation channels having an important role in crack initiation [1, 2].

Systematic research of strain localization in irradiated austenitic steels, performed in the framework of the LWRS program, revealed the overwhelming complexity of this phenomenon. Several specific irradiation-induced deformation mechanisms were found and investigated [12, 13], including the appearance of strain-induced martensitic phases associated with dislocation channels [12] and the formation of specific areas with high local misorientation (deformation “hot spots”) [13]. Other researchers demonstrated the role of dislocation channels as stress localization sites [14, 15].

At the same time, the experiments revealed limitations of the post-mortem (or post-test) analysis. For example, the structure of the specimen with and without applied external stress may be not the same. While minor differences in the dislocation structure may be neglected (this is typical), some materials may demonstrate de-twinning during external stress removal. For instance, Barnett et al. [5] conducted electron back scatter analysis of Mg-3Al-1Zn alloy and demonstrated [5] that stress release led to de-twinning; part of the deformation twins formed during straining.

Additionally, because of high yield stress in austenitic steels after irradiation, the elastic strains may be high enough to provide the driving force for dislocation channel evolution during unloading. This means that strain and stress distribution on the grain level may be different depending on the external loading conditions. This aspect is also important and worth investigating. The only way to avoid these issues is to characterize the structure continuously, in situ, without unloading the sample. In the past, in situ testing required special equipment, usually not available at the lab level, like neutron or synchrotron sources.

Recent progress in experimental techniques allows for precise Kikuchi diffraction (or electron back scatter diffraction [EBSD]) measurements to be made inside a typical scanning electron microscope (SEM), which greatly enhances the available experimental capabilities.

EBSD has developed into a very useful tool, with high-resolution EBSD (HR-EBSD) coming into practical use several years ago [6]. Because EBSD patterns are sensitive to the elastic strains, HR-EBSD allows for direct measurements of the acting stress and for calculating the geometrically-necessary dislocation density [6]. In a metallic polycrystal, local acting stress may be different than the applied macroscopic stress because of elastic anisotropy. Moreover, when measuring the sample under stress, one can find stress concentration points and connect them to structure features like grain boundaries and triple junction points [6, 5]. Currently, a limited number of publications are available for non-irradiated materials, but practically no work has been done for irradiated materials.

With the in-situ straining capability, one continuously-deformed specimen will be able to provide data for a wide range of conditions (e.g., strain levels). This approach was successfully used for in-situ creep experiments [7] and precise strain and misorientation mapping [8]. Taking these and other potential benefits into account, it was decided to establish similar capability at Oak Ridge National Laboratory's (ORNL) Low Activation Materials Development and Analysis (LAMDA) laboratory.

## 2. VERSA 3-D SEM: GENERAL DESCRIPTION AND SYSTEM PARAMETERS

The microscopy area of ORNL's LAMDA laboratory is equipped with two scanning transmission electron microscopes (STEM) and three dual-beam focused ion beam scanning electron microscope (FIB-SEM) instruments. One of these dual-beam FIB-SEM instruments—the FEI Versa 3D (Figure 1)—is a high-resolution imaging/analysis instrument. This particular instrument is equipped with a Schottky field emission gun (FEG), atop an electron column that can accelerate the generated electrons to energies of between 200 eV and 30 keV, with the ability to reduce the beam energy to 50 eV using beam deceleration. In imaging mode, the ultimate resolution of this instrument is 1.0 nm at 30 keV, although 0.8 nm point-to-point resolution is attainable using a STEM detector. Several electron detectors for imaging are available on this instrument, including an Everhard-Thornley secondary electron detector (ETD), an in-column secondary electron detector, a back scattered electron (BSE) detector, and a STEM detector.



Figure 1. General view of the VERSA 3D dual beam (scanning electron microscope and ion beam).

In addition to high-resolution imaging capabilities, the FEI Versa instrument also has the option to operate in *analytical* mode in which high electron beam currents (>4 nA) are achievable. Two detectors

are installed on the instrument that utilizes these high beam currents to enable detailed characterization of the local surface chemistry and phase analysis: (1) an energy dispersive x-ray spectroscopy (EDS) detector, and an EBSD. The EDS detector is an Oxford Instruments *X-Max<sup>N</sup>* with a 150 mm<sup>2</sup> solid-state detector. This detector provides quantitative and qualitative chemical information for most elements down to lithium. The EBSD system is based around an Oxford NordlysMax<sup>2</sup> high-efficiency platform for high-speed data acquisition. Both the EDS and EBSD are operated through the Oxford Aztec software system and can be operated independently or in parallel.

The FEI Versa instrument was selected to perform the in-situ testing of the tensile stage owing to its superior imaging and analytical capabilities. As such, the tensile stage was designed around this EM platform.

### 3. MINIATURE TENSILE STAGE FOR IN-SITU TESTING

The following criteria were considered for selecting an in-situ test system:

- compatibility with the existing microscope and EBSD system
- high loading capacity and ability to handle both tensile and compression tests
- ability to work at elevated temperature
- upgradeability (gear boxes for extended strain rates, cooling stage availability, etc.)

Several vendors provide miniature tensile stages; however, not all of the available tensile stages are compatible with the VERSA 3D SEM. Some systems had limited loading capacity (1 or 2 kN), which limits the available test schemes. After analyzing the options available on the market, Kammrath and Weiss Technologies, Inc. was chosen as the supplier for the miniature tensile stages. Kammrath and Weiss Technologies, Inc. specializes in the development and production of custom-made systems for mechanical testing under specific conditions (e.g., vacuum, high- or low-temperatures, corrosive environments). The tensile stage was purchased through a cooperative effort of several programs (LWRS, Fuel Cycle Research & Development [FCRD] program, and the Nuclear Energy Enabling Technologies [NEET] program).

The tensile frame (Figure 2) was delivered and installed in the VERSA SEM in December of 2016. Several trial in-situ tests conducted inside VERSA SEM demonstrated that the working distance (the distance between the sample and the electromagnetic lens) might be as small as 15.5 mm, which provides good resolution and a high-quality EBSD pattern. The tensile frame has a maximum loading capacity of 5 kN and a maximum strain rate of 50  $\mu\text{m}$  per second (3 mm per min). Two force sensors (one with a 5 kN range and one with a 2 kN range) were ordered to support testing of miniature tensile specimens for the ongoing projects and to conduct mechanical fracture tests in the future.

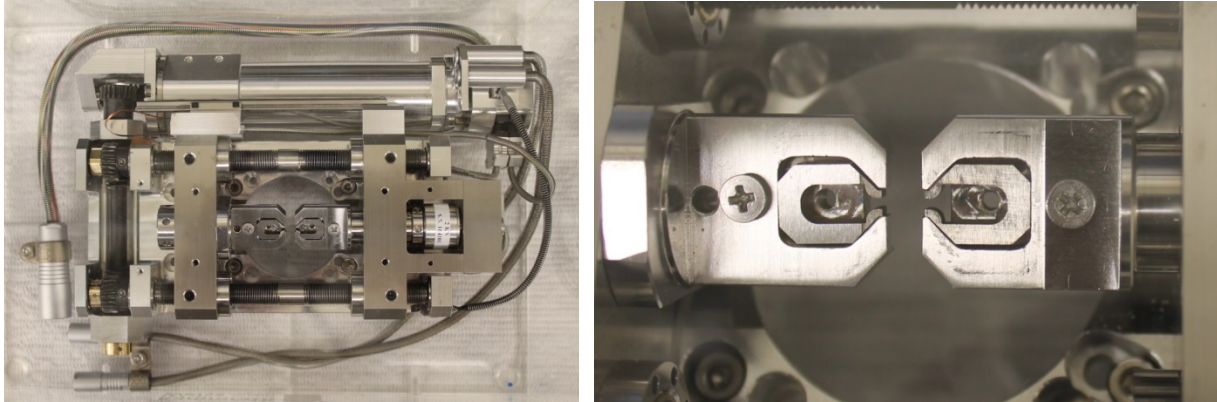


**Figure 2. Left: General view of the tensile stage (Kammrath and Weiss Technologies, Inc., Model MZ.Sb). Right: the enlarged image of the grips with holders installed for SS-J specimen geometry.**

The selected heating stage (Figure 3) allows for a maximum temperature of 800 °C in a vacuum (or 400 °C in open air, [outside the SEM]). Preliminary tests demonstrated the system's stability at elevated temperatures and low thermal inertia. However, implementing high-temperature testing will require additional careful work to ensure a uniform temperature field across the specimen gauge. Good thermal contact and uniform temperature distribution may be of concern with strain level increase during the in-situ test. Strain-induced surface roughness will likely lead to reduced thermal contact between the heater and specimen.

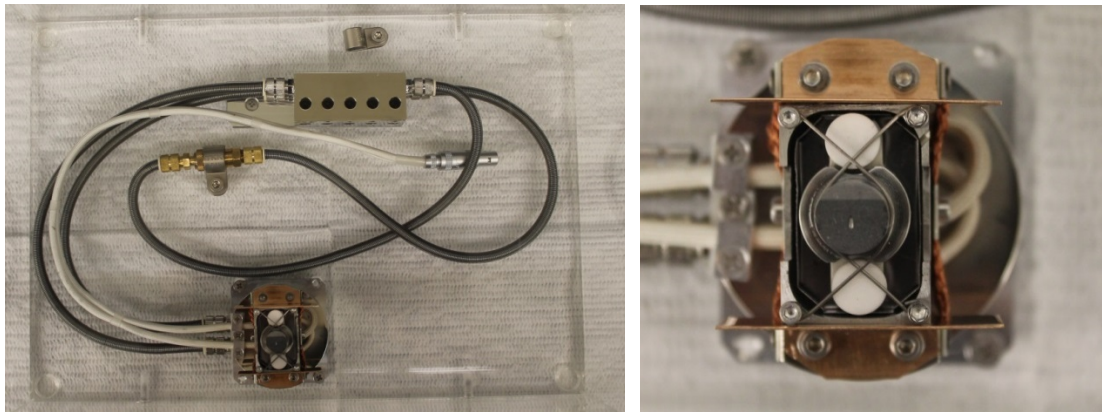


**Figure 3. General view of the heater (left) and the enlarged view of the heating element (right).**

As shown in Figure 4, the system control units (computer, tensile stage controller, temperature controller, and water chiller) were mounted on the cart to provide a high degree of mobility.

Mechanical testing inside the SEM did require a special, separate radiation work permit to cover new risks associated with destructive testing and specimen fracture; preparation of the necessary documents is in progress.

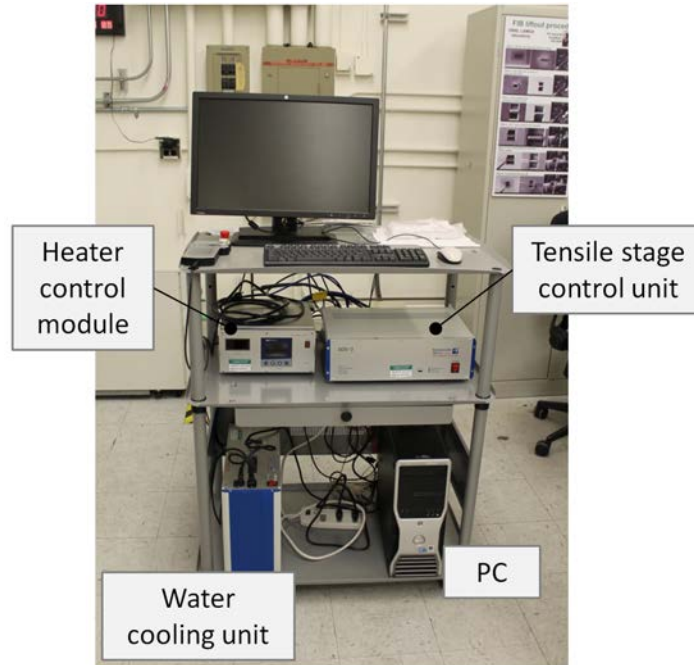


Figure 4. Tensile stage control modules located on the cart.

## 4. SPECIMEN DESIGN AND PRODUCTION

### 4.1 AVAILABLE IRRADIATED MATERIALS

The LAMDA facility has assembled a library of irradiated materials from both active and completed programs. For instance, the inventory of available specimens includes irradiated materials (more than 12 austenitic alloys) produced as part of the Cooperative IASCC Research (CIR) program [9, 10, 11, 1], which was active between 1996 and 2010. The CIR samples were irradiated in the BOR-60 reactor, and details on this irradiation campaign may be found in [10]. Some of the irradiated tensile specimens were tested at the University of Michigan in 2010–2014. The key results from the tensile specimens and constant extension rate tests (CERTs) were published by several authors [11]. As expected, the legacy materials from the CIR program may serve as a source of irradiated 304L and 316L steels.

These samples may be modified to produce sub-size specimens for different purposes, including in-situ tensile experiments. The low dose ( $\sim 4.4$  dpa) annealed 304L steel (SW alloy) looks like the most promising material because of a well-established history of published results on its structure and properties.

Additionally, several highly-irradiated samples of 304L steel were purchased recently by the LWRS program. The samples were cut from bulk hex blocks that were irradiated at a maximum dose of  $\sim 35$  dpa in the EBR-II fast reactor. As expected, the samples (thin plates with a dimension of  $\sim 12 \times 12 \times 0.5$  mm) will be delivered in March of 2017.

### 4.2 SPECIMEN GEOMETRY

In most cases, the geometry of the available irradiated object does not allow for producing standard SS-3 or SS-J specimens. Taking into account the shape and dimensions of the available irradiated objects (e.g., plates of  $\sim 7 \times 3.5 \times 1$  mm), a miniature specimen design was developed for this particular case.

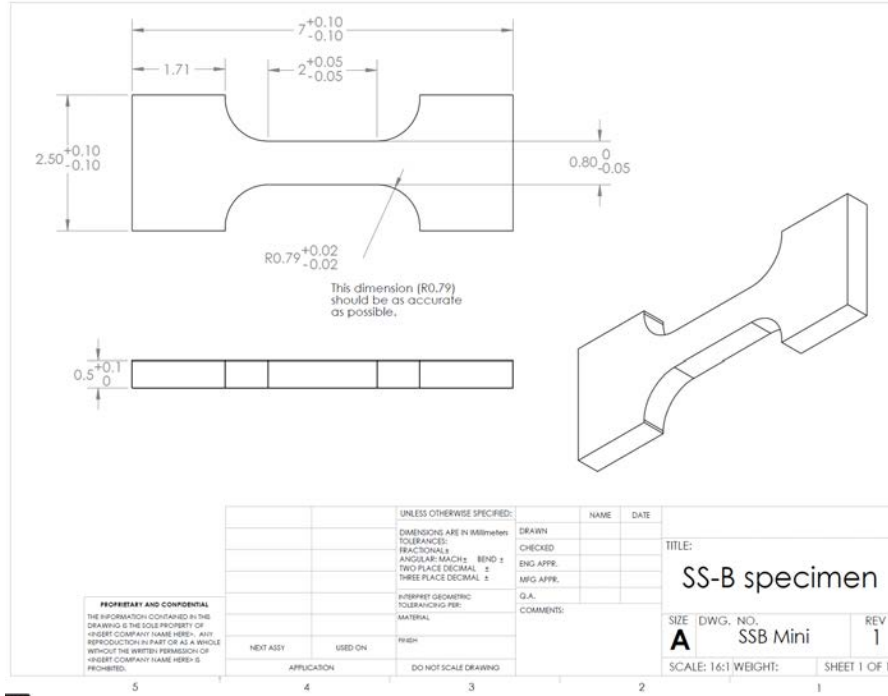


**Figure 5. Geometry and dimensions of the ultra-miniature specimen for in-situ testing.**

As expected, the geometry will accurately reproduce yield and ultimate stress values for the standard, larger specimens like SS-J. Behavior at small strain levels should be comparable to the bulk specimens with larger work volume; however, the ductility level may be smaller compared to the SS-J geometry, and the difference may depend on the strain level. This aspect will be evaluated later in detail in the future.

### 4.3 SPECIMEN FABRICATION APPROACH

Manufacturing hot samples from previously irradiated materials at ORNL’s LAMDA facility has significant cost benefits. Equipment (e.g., a milling machine) should be simple to operate, easy to repair and replace, and affordable. At the same time, acceptable accuracy/reproducibility is mandatory. The machine should also be small enough to fit a typical LAMDA hood. Specimen production should require minimum hands-on operations and be safe from a radiation control point of view.

After research and analysis of different machines on the market, a miniature 3-axis computer numeric control (CNC) machine (Figure 6) was purchased. The system passed all necessary safety control steps, has a certification from a Nationally Recognized Testing Laboratory (NRTL) and is now undergoing initial testing. A computer-aided design (CAD) program was developed to produce a miniature rectangular “dog-bone” specimen with a gauge width of 0.9 mm and gauge length 2.0 mm (Figure 5). Total specimen length will be around 7 mm and may vary depending on the available material. According to preliminary results, specimen machining (see the movie frames in Figure 6) takes around 50–55 minutes. After machining, specimen preparation to the in-situ test may be performed using well-established procedures (mechanical grinding and electropolishing).

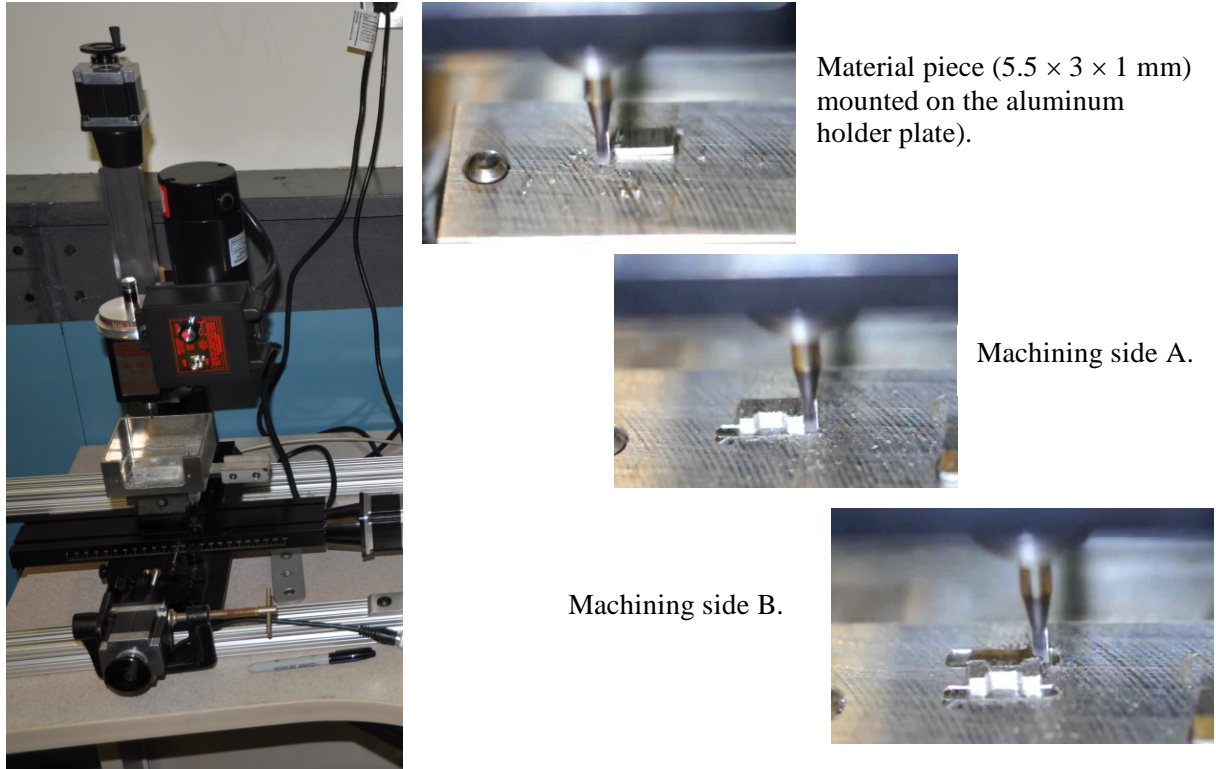


**Figure 6.** Sherline CNC milling machine, model 2010 (at the left) and specimen manufacturing steps (at the right). Images of the machining are slightly blurry because this process is performed in a water-filled container.

Several testing runs were conducted using 6061 aluminum alloy, annealed and cold-worked 304 steel, and—as a material with ultimate strength—precipitation-hardened 718 alloy. Promising results were obtained, and it was shown that a miniature tensile specimen (Figure 7) can be produced even from 718-alloy with a yield stress of around 1,200 MPa.

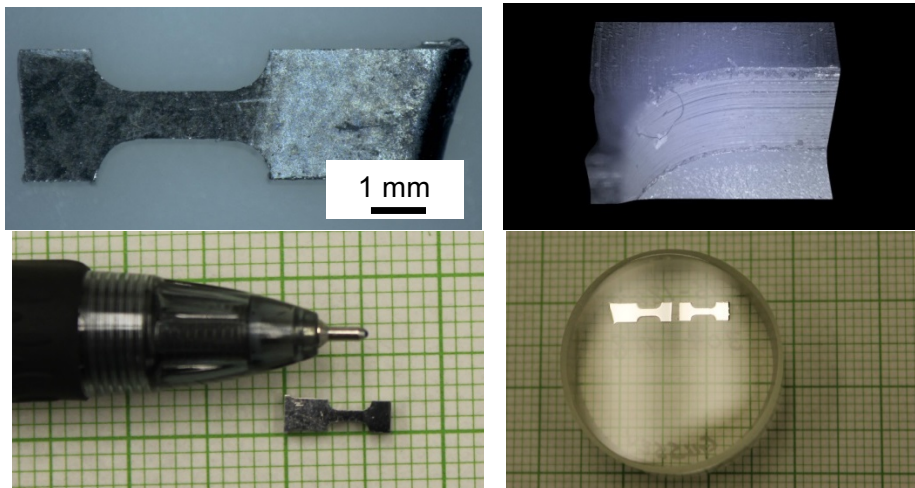


**Figure 7.** A 718-alloy miniature specimen (left), a 3D-image of typical tool marks on the specimen edge (top right), and miniature specimens mounted in epoxy (bottom right).

The CNC machine is currently being installed in the LAMDA lab, and if all goes as expected, the first trial cuts of irradiated material will be conducted in February–March of 2017.

## **5. PRELIMINARY RESULTS OF THE IN-SITU TESTS**

### **5.1 INTRODUCTION**

Austenitic 300-series steels, like American Iron and Steel Institute (AISI) 304 and 316 along with their numerous variants, are widely used in the nuclear industry because of their favorable combination of mechanical and corrosion properties and acceptable radiation tolerance. However, these materials are susceptible to a number of degradation mechanisms, with IASCC being one of the most severe issues associated with this class of materials [1, 2, 3].

IASCC is a complex process with many contributing factors [1]. Recently, plastic strain and dislocation channeling, leading to deformation localization, have been recognized as playing an important role in increased IASCC susceptibility [1, 2]. However, despite significant literature on the strain-induced phenomena in irradiated austenitic steels, the understanding of this process is still limited, especially for materials irradiated with high, damage-inducing doses. Thus, investigating plastic deformation processes in highly-irradiated materials may be important from a practical viewpoint. Employing new advanced test methods like in-situ testing with EBSD analysis may prove even more important and fruitful.

This section describes some preliminary results for an in-situ tensile experiment performed using the new tensile stage. The test was conducted using a non-irradiated tensile specimen of austenitic 304L steel. The test had several purposes. First, it was important to ensure that the new system—the SEM combined with the tensile stage—worked perfectly and could provide the expected outcome (reliable microstructure data coupled with stress and strain values). Second, the system performance had to be evaluated; it was important to find a realistic compromise between EBSD scan size, step size, the time required to perform scanning at given strain level, and the overall experiment time. EBSD pattern quality, as a function of strain level, had to be evaluated as well. Third, testing non-irradiated specimens will provide a baseline for their irradiated analogy.

### **5.2 TESTED MATERIAL**

A nuclear-grade, high-purity AISI 304 austenitic stainless steel was used for the in-situ trial tests. The test material was modified in the laboratory through induction melting in a vacuum. As the final thermo-treatment, the plates of SW'-alloy (nuclear-grade, high-purity 304L steel) were annealed at 1050 °C and quenched in water. After annealing, the material had a structure of annealed austenite with zero ferrite retained. The average grain size was around 57 μm for the un-irradiated alloy. The element composition (Table 1) was verified by the off-site commercial vendor.

The material is designated as “SW'-alloy” (or “SW'-heat”) in the present work. The SW'-heat is expected to serve as a reference heat for several groups of irradiated 304L steels. For example, specimens of high-purity, nuclear-grade 304L steel (designated in several reports as “SW-alloy”) were produced by a Swedish company and irradiated in the BOR-60 fast reactor. Considering the moderate-damage dose (4.4 dpa) and low activity, the SW-alloy samples are a natural choice for the in-situ testing in the near future.

The non-irradiated specimens of SW'-heat have a very close elemental composition (Table 1) and grain size and thus serve as reliable reference objects for the neutron-irradiated SW-alloy (4.4 dpa).

**Table 1. Composition and condition of material investigated**

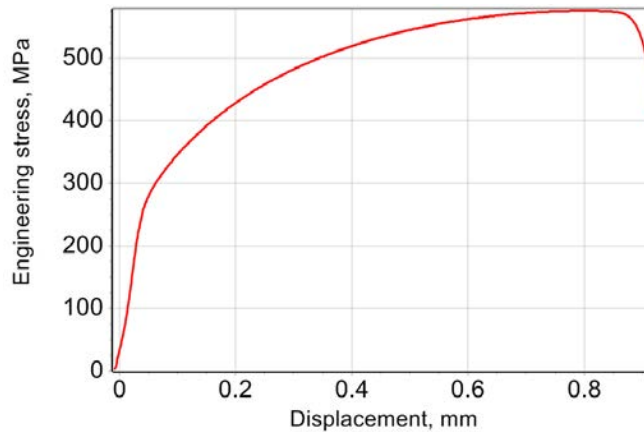
Alloy	Fe	C	Mn	Si	Cr	Ni	Mo	N	Grain size ( $\mu\text{m}$ )	Purpose
SW'	Bal.	0.016	1.03	0.24	18.39	10.45	0.0013	0.056	57	Non-irradiated reference material
SW	Bal.	0.022	1.07	0.24	18.42	10.45	0	0.025	67	4.4 dpa at 320 °C in the BOR-60 fast reactor

### 5.3 MECHANICAL BEHAVIOR

The SW'-alloy specimens were tensile tested prior to the in-situ experiment to provide the baseline on the mechanical properties. The results, low yield stress and high ductility (Table 2), are typical for annealed austenitic 300-series steel. The tensile curves (Figure 8) were smooth and had no specific peculiarities (e.g., yield drop).

**Table 2. Mechanical properties of the SW'-alloy**

Yield strength (0.2% offset) (MPa)	Ultimate strength (MPa)	Uniform elongation (%)	Full elongation (%)
253	579	69.2	81.2

**Figure 8. The representative tensile curve for the SW'-alloy (annealed nuclear-grade 304L steel).**

### 5.4 IN-SITU TEST AND SURFACE TOPOLOGY EVOLUTION

The in-situ test was conducted with an active grip displacement rate of  $1 \mu\text{m/s}$ , which corresponded to the strain rate of around  $5 \times 10^{-4} \text{s}^{-1}$ . The selected strain rate value was smaller than the common strain rates typically used in tensile experiments ( $\sim 10^{-3} \text{s}^{-1}$ ) and was selected for the trial for testing purposes only.

The tensile sample was loaded into the grips, and the central gauge portion was EBSD-scanned to provide reference data (Figure 9). The EBSD detector was not fully inserted because the loaded tensile stage limited the available space. To minimize the risk of damaging the detector, scanning was performed with a detector located at the “204 mm” position instead of the standard “219 mm” position. In other words,

the distance between the detector and specimen's surface increased by 15 mm. Although still within formally-allowed limits, the increased distance led to a slight decrease in quality for the EBSD data, and some grains were not indexed properly (Figure 9).

At the same time, EBSD pattern quality was high enough, and the indexation rate in the  $2 \times 2$  binning mode reached around 100 points per second. In the future, the working distance (WD)—the distance between the SEM pole and the specimen—may be increased from 15.5 up to 17 mm to allow for better/risk-free EBSD detector positioning.

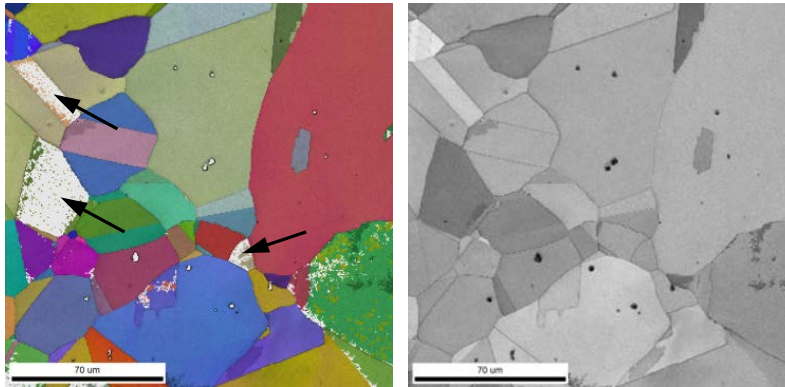


**Figure 9. EBSD IFP and image quality (IQ) maps for the reference area prior to deformation. Black arrows show non-indexed grains.**

After reference location scanning, the specimen was deformed with a strain rate of around  $5 \times 10^{-4} \text{ s}^{-1}$ . The tensile test was interrupted several times, and EBSD scans were conducted for the same area. One of the goals was to analyze the small strain range ( $<1\%$ ) to assess the possibility of detecting strain-induced changes near yield stress. Several stops were performed in the moderate-strain area ( $<20\%$ ), and finally, large strain increments were performed to establish the level of EBSD data degradation that occurs as strain increases and to determine the largest strain level achievable while still obtaining useable EBSD data. After each strain increment, the specimen was partially unloaded before the EBSD scanning to minimize the creep-related effects. Figure 10 shows tensile curves for conventional and in-situ testing.

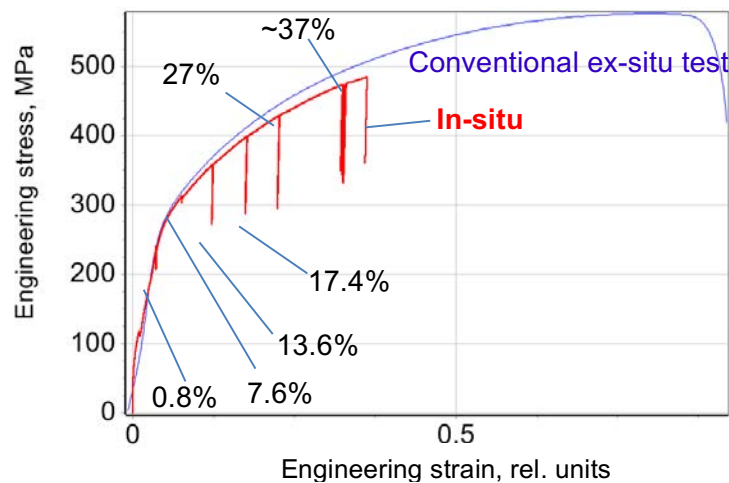


**Figure 10. The tensile curve from the in-situ test (thick red line) compared to results from the ordinary tensile test (thin blue line). Partial unloading was performed during EBSD scans to minimize the creep-related effect. For some cases, local strain levels for the area of interest are shown.**

SEM images, as shown in Figure 11, were taken for each strain level to analyze the surface evolution and to estimate the local strain level. Strain-induced surface evolution is clearly visible. While weak slip lines presented at the surface at 0.8% strain, a strong increase in the slip line density was observed at 7.6% strain, and multiple active slip systems acted in the same grain at larger strains. Grain rotation and surface relief formation became evident at a few percent of strain. Interestingly, non-metallic inclusions visible on the electro-polished surface survived up to a high strain level, which allowed for a clear and easy identification of the area of interest.

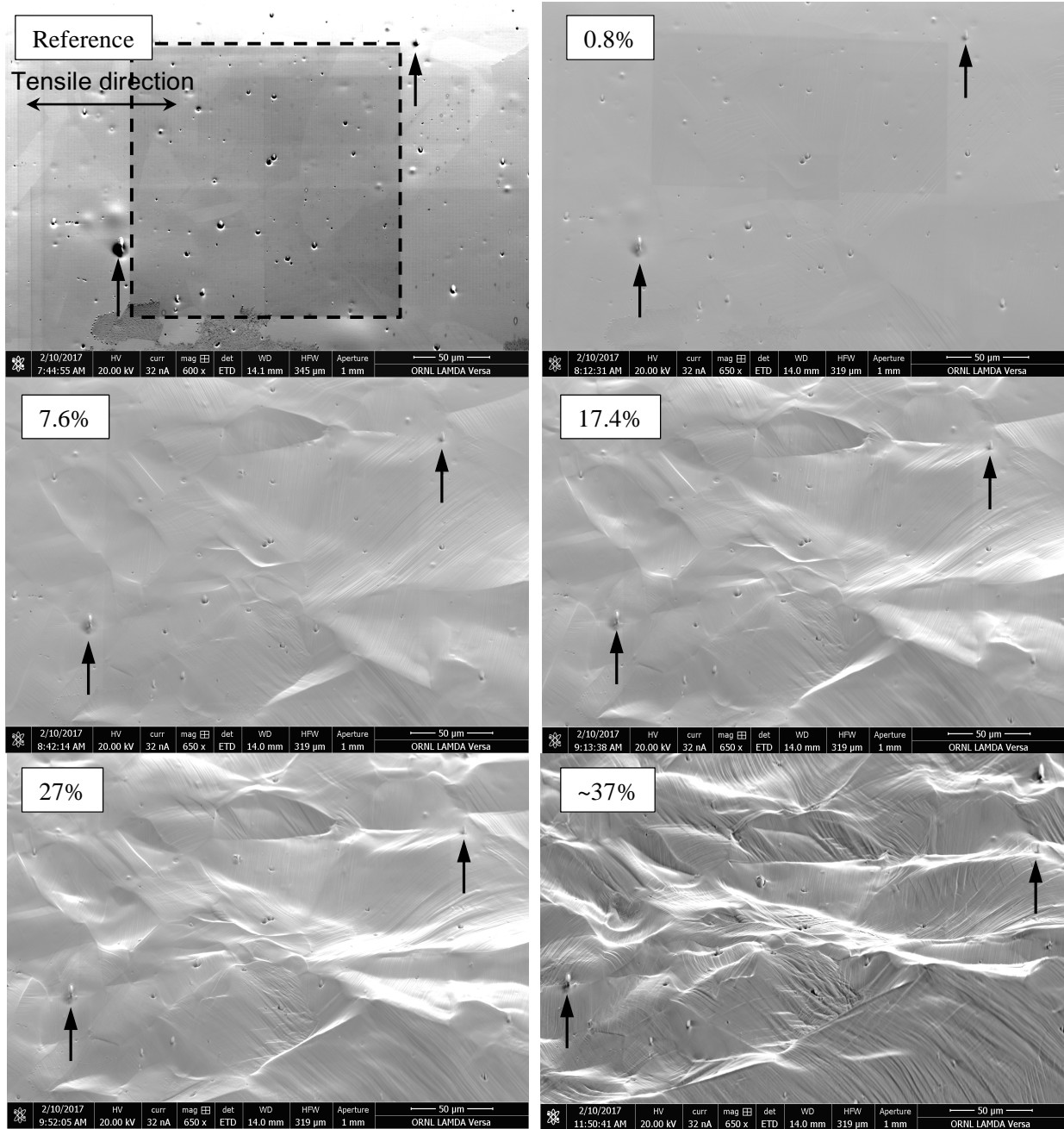


**Figure 11. SEM images taken at different strain levels.** The above images depict the surface topology evolution from single slip lines to a pronounced strain-induced relief. Black arrows track the pair of inclusions through the images. The dashed rectangle identifies the area of interest. Note that there are some variations in the magnification level.

## 5.5 ANALYSIS OF THE EBSD MAPS TAKEN DURING THE IN-SITU TEST

Figure 12 shows the evolution of the EBSD maps as the strain level increased. The EBSD's data quality remained acceptable within small and moderate strain ranges (<20%). The preliminary test was able to reproduce all specific strain-induced phenomena described in the literature: grain rotation, grain fragmentation, and an in-grain misorientation increase. Grains with an initial orientation close to [101] rotated towards the [001]–[111] line, and their color changed in the inverse pole figure (IPF) map. In-

grain orientation increased significantly, which led to a strong increase in the maximum misorientation values observed in the grain reference orientation deviation (GROD) maps (from about  $5^\circ$  at 0.8% up to about  $27^\circ$  at 13.6%).

As the strain level increased and exceeded 20%, as depicted in Figure 13, the EBSD map quality started to degrade drastically. Many areas became invisible for the EBSD detector because of the grain rotation and strain-induced roughness. Nevertheless, many grains still appeared in the resulting maps, which provided an opportunity to analyze the large strain levels, if necessary.

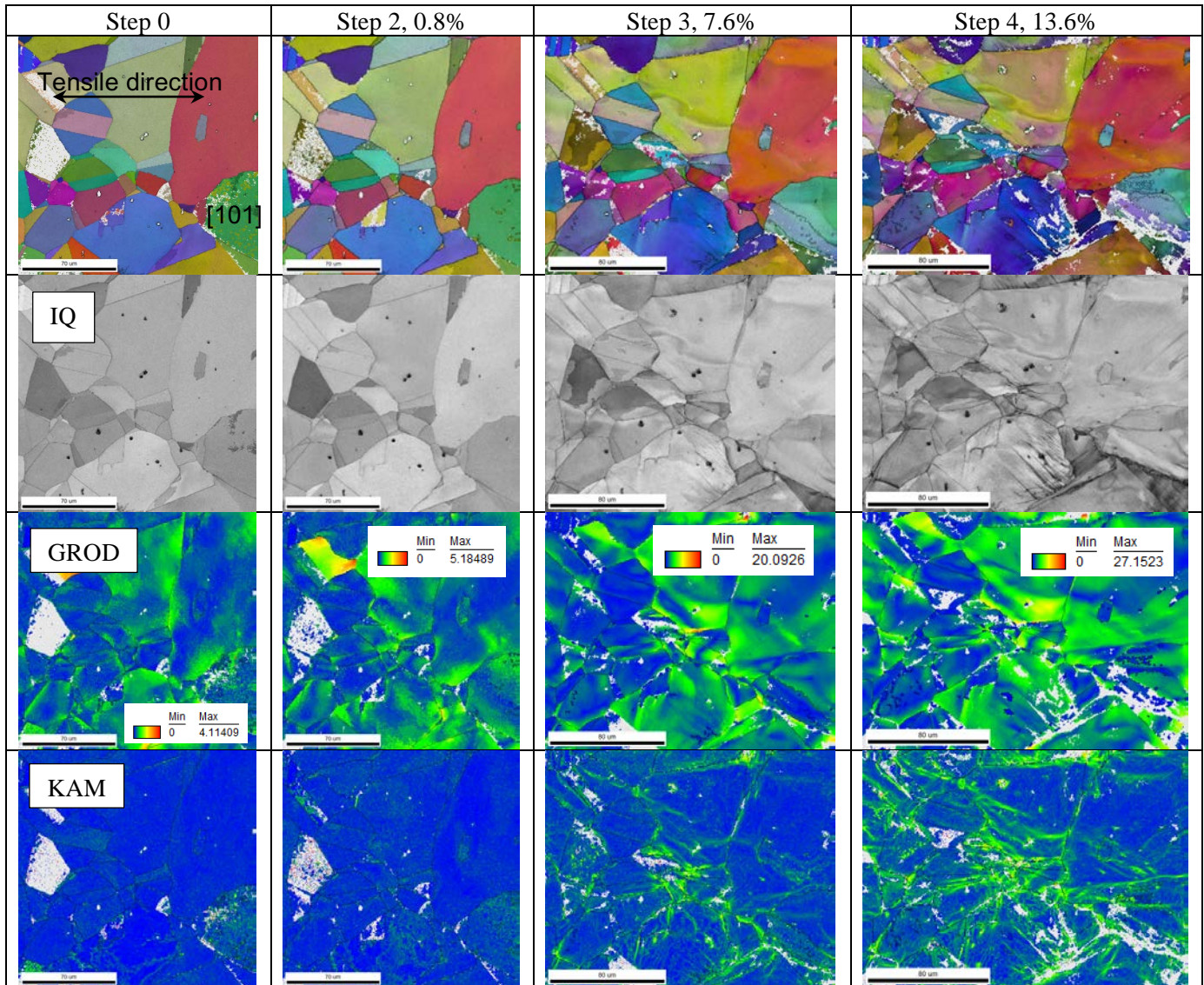


**Figure 12. Evolution of the IPF (colored in the tensile direction), IQ, GROD, and kernel average misorientation (KAM) maps for the same area at different strain levels.**

Decreasing the distance between the specimen and the EBSD detector may improve the indexation quality but at the cost of the working distance and overall resolution. Further evaluation of this tradeoff will be presented in future work.

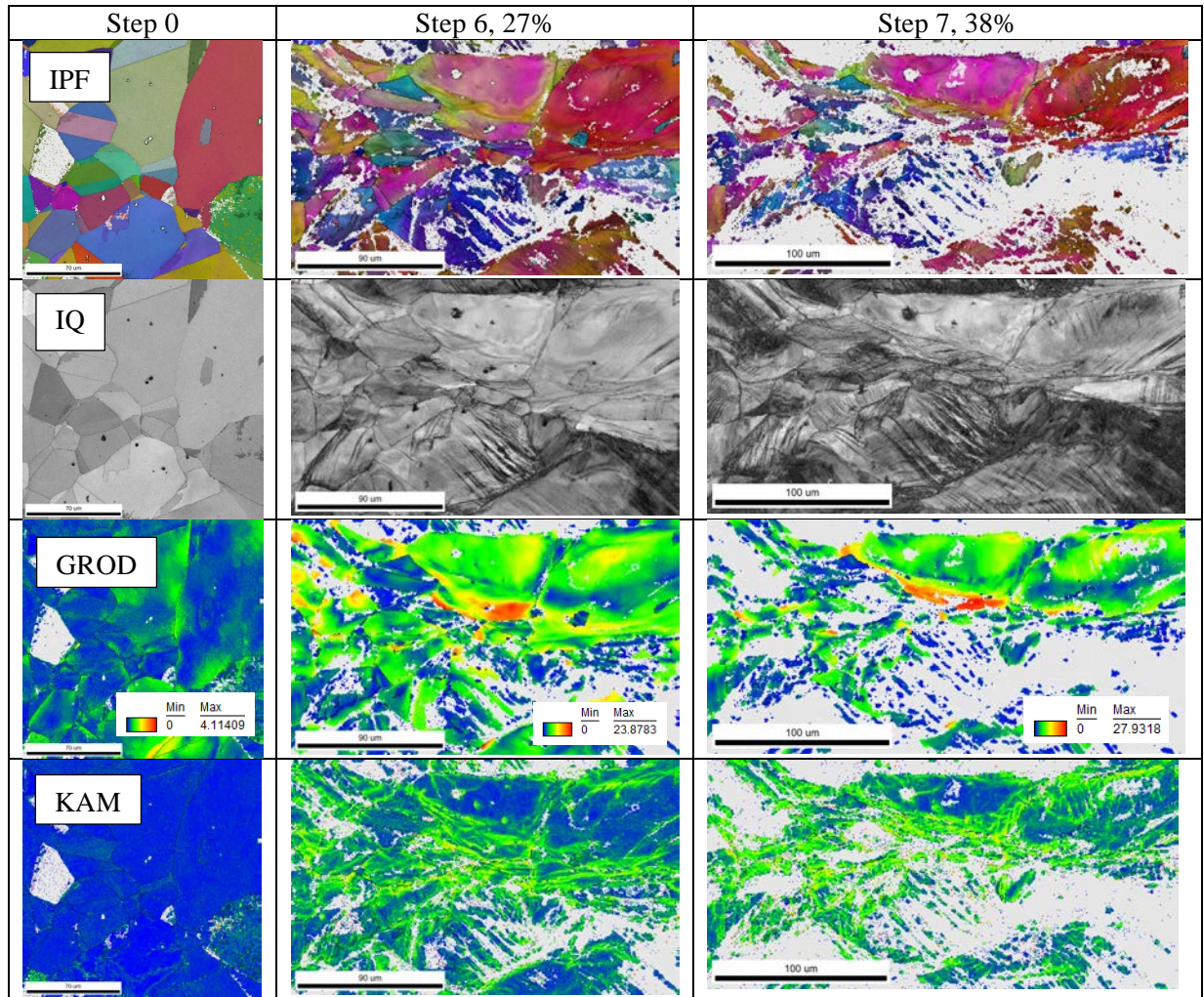


**Figure 13. Degradation of the EBSD data at large strains compared to the reference image (Step 0).** Strain values were calculated from SEM images taken at the same location using the same imaging conditions (working distance and magnification).

## 5.6 EBSD IMAGE QUALITY EVOLUTION

Figure 14 shows the EBSD data quality (fraction of successfully indexed points) as a function of local strain level. As shown, most of the area of interest was successfully scanned (>80% of the points of interest) at strain levels below 20%. At smaller strain levels (0%–10%), grain rotation and strain-induced relief were not as pronounced, and EBSD data quality remained high.

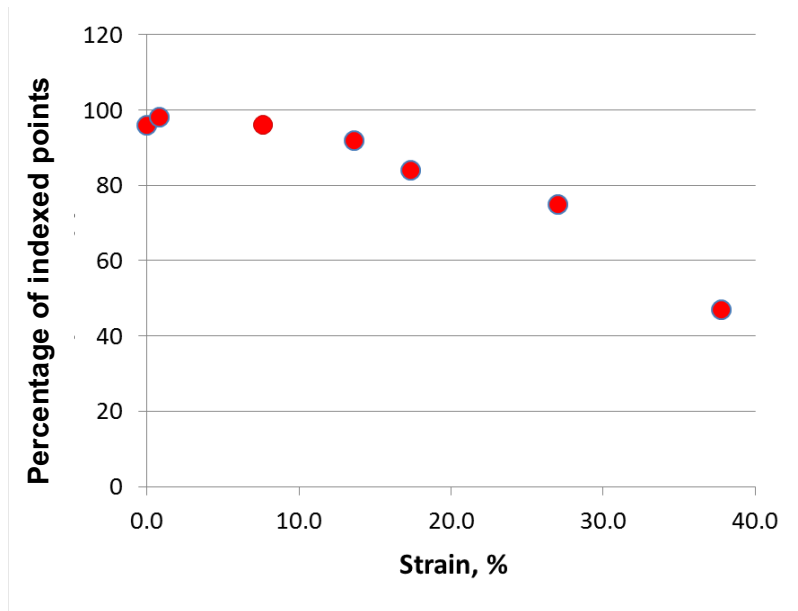


**Figure 14. EBSD data quality (fraction of “good points”) as a function of local strain level.**

### 5.7 EBSD STRAIN METRIC ANALYSIS

The most common EBSD strain metrics—GROD and KAM—were calculated for the reference area shown in Figure 9 and then EBSD scanned at different strain levels. The maximum GROD values (the largest increase in the grain deviation from some reference value) increased linearly with the strain level. Starting at a strain level of about 15–17%, the maximum GROD values tended to saturate because of grain fragmentation and the appearance of in-grain, high-angle boundaries within the grain. It appears that below this 15–17% strain level, the GROD maps may be used to estimate the local strain level if a sufficiently large EBSD map ( $180 \times 180 \mu\text{m}$  with ~30–50 grains) is available.

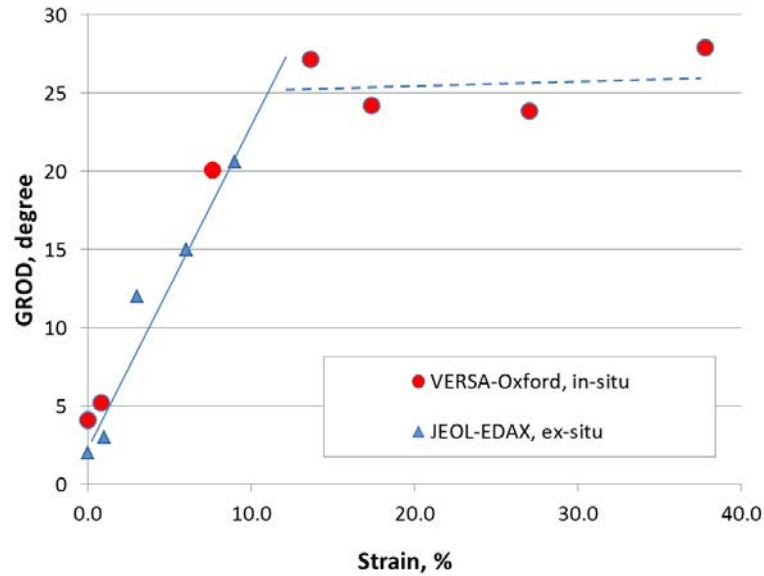


**Figure 15. GROD as a function of the strain level.** In situ data (round markers) are compared with ex-situ test data (triangles); step size was the same for both at 0.5  $\mu\text{m}$ .

The KAM value also increased linearly with the strain level up to around 20% strain (Figure 16). After that, the KAM value continued to increase but at a shallower rate/slope. The linear relationship between KAM and strain level agrees with the literature and allows for estimating the local strain values, at a given location, if the reference value and the correlation curves are known.

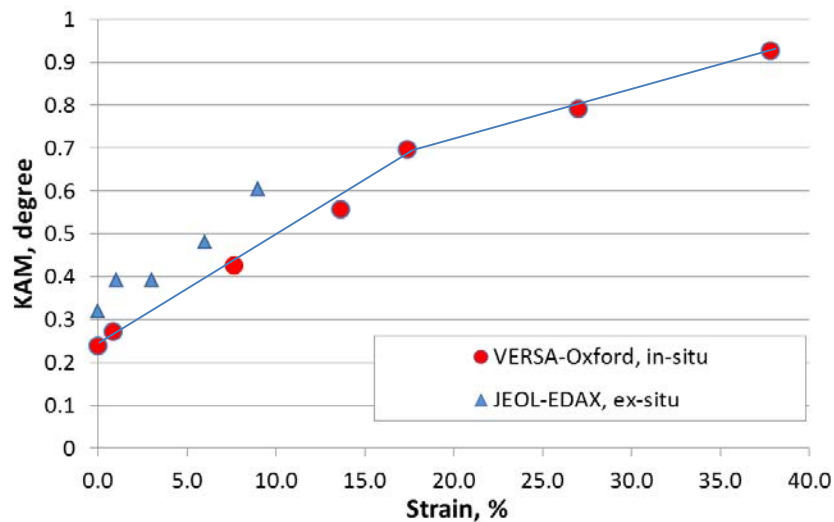


**Figure 16. Evolution of the KAM parameter as a function of the local strain level.** The in situ data (round markers) are compared to ex-situ data (triangles) obtained earlier using a different system (JEOL 6500F+ EDAX EBSD); step size was the same for both at 0.5  $\mu\text{m}$ .

The in-situ test results were compared with the ex-situ tests performed earlier. In this case, a series of tensile specimens were deformed at room temperature, mechanically grinded, electropolished, and then EBSD scanned using a different system—a JEOL-6500F equipped with an EDAX EBSD detector. As

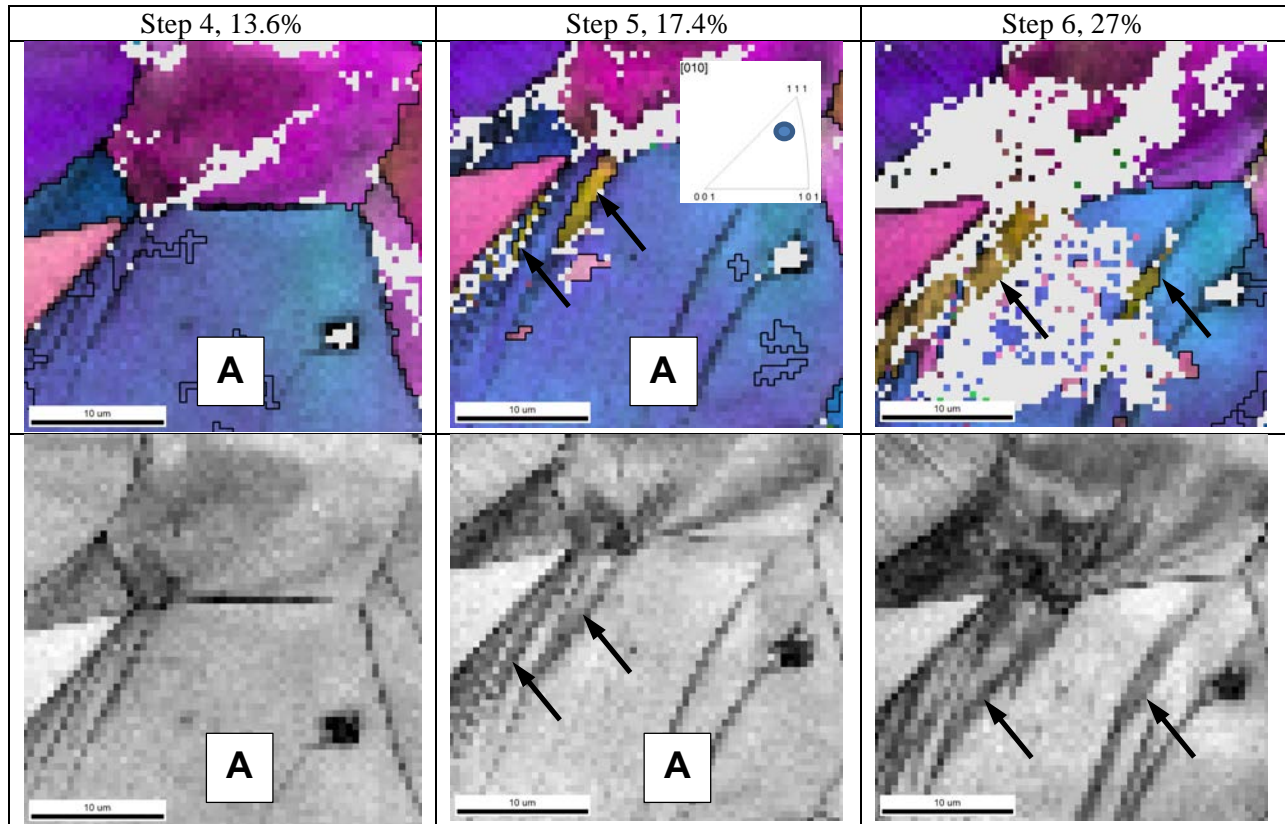
shown in the results (Figure 15 and Figure 16), the strain-induced changes in the GROD parameter were close enough for both in-situ and ex-situ tests. The KAM parameter has a similar slope, but the curve was shifted up slightly. Good agreement between the in-situ and ex-situ (post-mortem) test results shows the reliability of the EBSD data obtained on a single specimen deformed in step-by-step mode.

It is important to note that the GROD and KAM curves for the in-situ test case were obtained from a single specimen, thus minimizing the number of required specimens for the experiment; sourcing multiple specimens of irradiated material can be prohibitively expensive. Furthermore, specific defect-to-defect interactions may be easily tracked with the in-situ method.

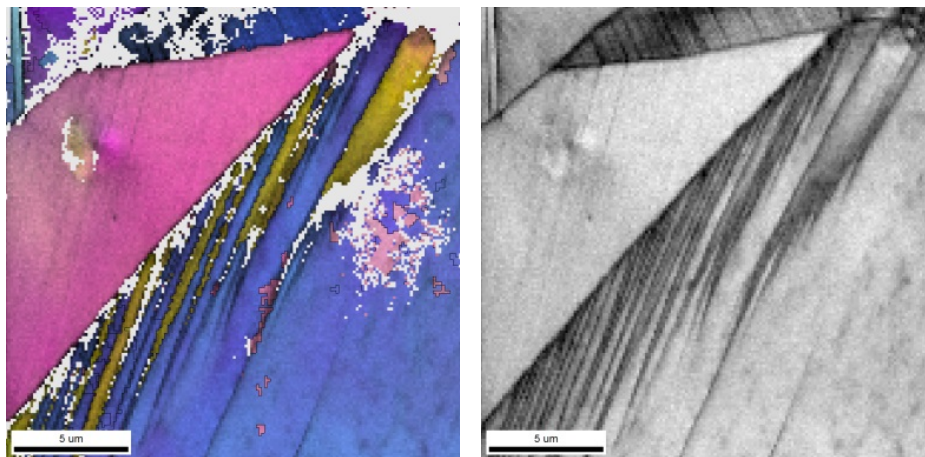
## **5.8 STRAIN-INDUCED PHENOMENA IN AUSTENITIC STAINLESS STEEL**

Figure 17 shows an appearance and evolution of the deformation twin. The EBSD map (fragment of the general IPF map shown in Figure 9 and Figure 12) demonstrates the twin-free grain at 13.6% strain (left), the appearance of several strain-induced twins at 17.4% strain, and their growth coinciding with the strain level increase.

Note that the strain-level and external stress-induced twin formation may be defined more precisely—or at least more accurately—compared to the ex-situ post-test analysis. At the same time, grain orientation regarding the external stress direction may be easily defined. Also note that the IQ map with visible grain boundaries allows for a clear delineation between simple slip lines and areas containing deformation twins (twins appear to be darker). In other words, IQ maps provide an additional way to confirm the observed phenomenon (e.g., twinning).



**Figure 17. Deformation twin appearance and evolution with strain increase.** Grain A was twin-free at 13.6% strain, and a clear indication of the strain-induced twin (black arrows) appeared during the next strain increment (Step 5, 17.4%). With another strain increment (Step 6, 27%), the twins grew, and an additional twin appeared in a different area. Also note the strong increase in the non-indexed point fraction.



**Figure 18. EBSD data for the area shown above.** Scanning was performed at 1500 $\times$  magnification with a 125 nm pitch (Step 5, 17.4%). Shown are fine deformation twins in addition to the coarse deformation twins visible in the 0.5- $\mu$ m scan.

If necessary, any location may be scanned at higher magnification and with higher resolution to provide more details on the phenomenon of interest. An example is given in Figure 18 where a high-resolution (125 nm) scan reveals additional fine twins not visible in the scans performed with the 0.5  $\mu\text{m}$  step.

Figure 19 illustrates another interesting case: in-grain misorientation and grain rotation. Here, two grains (A and B depicted in Figure 19) were selected and isolated in a separate data set. The evolution of these two grains was tracked through different strain levels. Prior to straining, the grains had a very low in-grain misorientation level and orientation spread (see the unit triangles). At 7.6% strain, points belonging to the selected grains formed a specific halo around the initial location. For most points, deviation from the original orientation was within  $3^\circ$ – $5^\circ$ ; however, several points shifted up to  $10^\circ$ – $15^\circ$  forming an elongated “tail.” The grain rotation direction was fairly random at smaller strain levels; however, at larger strain levels, rotation towards the  $[001]$ – $[111]$  direction became the norm.

This phenomenon—grain rotation, in-grain orientation spread, etc.—is weakly explored in the irradiated materials. Owing to a high degree of strain localization in irradiated materials, one may expect grain rotation to be more pronounced or accelerated as the strain level increases.

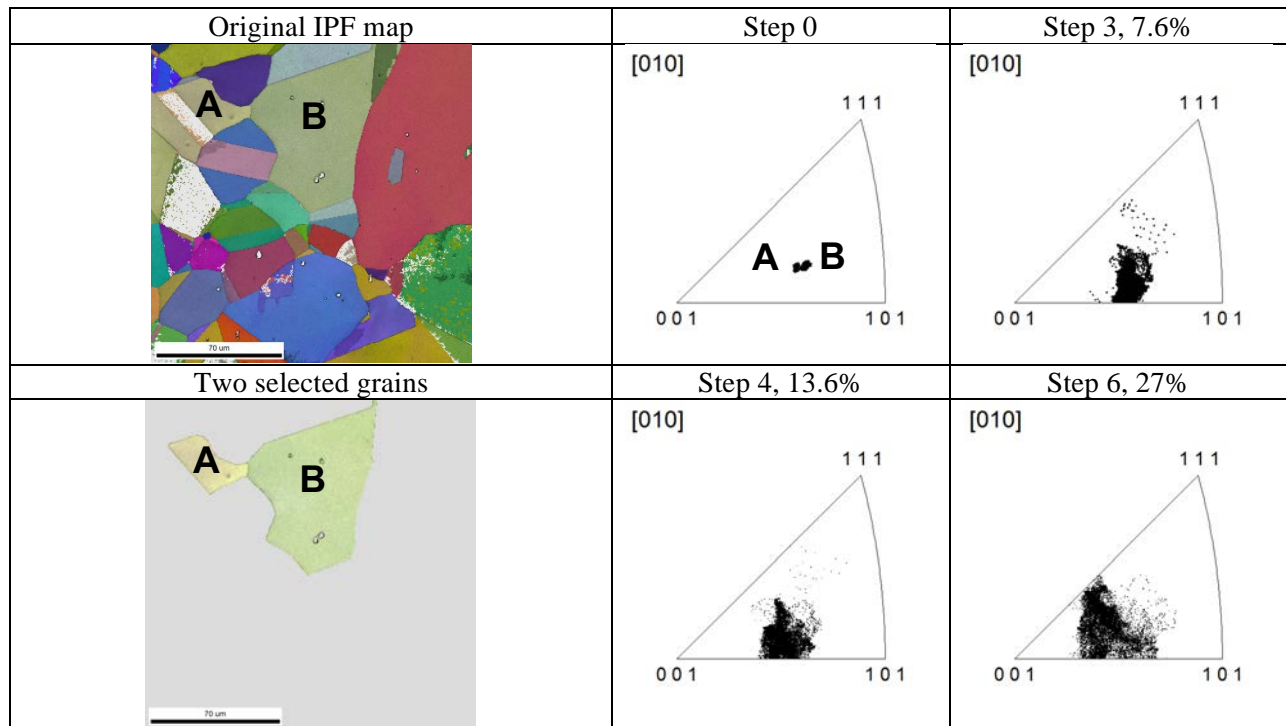


**Figure 19. An example of grain rotation behavior.** Two grains (A and B) were moved in a separate partition. During straining, there is a strong increase in the in-grain spread, but the general tendency is to rotate towards a  $[001]$ – $[111]$  line.

## 6. SUMMARY AND CONCLUSIONS

An advanced mechanical test method was implemented at ORNL’s LAMDA facility to test miniature irradiated specimens. A small tensile frame with a 5 kN loading capacity was purchased, delivered, and installed inside the VERSA 3D SEM. The tensile frame allows for both tension and compression modes and has a heating stage that provides temperatures up to 800  $^\circ\text{C}$ . Designing custom grips will enable the tensile frame to accommodate most schemes, including tensile, compression, and fracture mechanics testing. The SEM includes EBSD and EDS detectors, as well as focused ion beam capability. This

development, coupled with LAMDA's ability to handle and prepare irradiated objects, provides a set of unique opportunities for mechanical testing of irradiated specimens.

In the present report, some preliminary testing was conducted using non-irradiated 304L steel—a reference material for irradiated specimens already available at LAMDA. The in-situ tensile test confirmed the possibility to track, scan, and investigate the selected area by analyzing changes in local misorientation, grain rotation, slip line development, and appearance and evolution of strain-induced twins.

Future activity will include tensile testing of the irradiated specimens. Initially, these tests will be conducted at room temperature, but will eventually be tested at LWR-relevant temperature ranges.

## 7. ACKNOWLEDGMENTS

The present research was sponsored by the U.S. Department of Energy, Office of Nuclear Energy, for the Light Water Reactor Sustainability Research and Development Effort. The tensile frame purchasing was a cooperative effort of several research and development programs and projects being performed at ORNL: LWRs (K. Leonard), FCRD (K. Terrani), NEET (K. Field), and others; the contribution of these programs is greatly appreciated. The authors would also like to thank Dr. K. Terrani (ORNL), Dr. K. G. Field (ORNL), Dr. Y. Kato (ORNL), and Dr. L. Tan (ORNL) for the fruitful and stimulating discussions and S. Crawford (ORNL) for his valuable help with document preparation.

This manuscript has been authored by the Oak Ridge National Laboratory, managed by UT-Battelle LLC under Contract No. DE-AC05-00OR22725 with the U.S. Department of Energy. The U.S. Government retains and the publisher, by accepting the article for publication, acknowledges that the U.S. Government retains a nonexclusive, paid-up, irrevocable, worldwide license to publish or reproduce the published form of this manuscript or allow others to do so, for U.S. Government purposes.

## 8. REFERENCES

1. Was, G. S., Y. Ashida, and P. L. Andresen. 2011. "Irradiation-Assisted Stress Corrosion Cracking." *Corrosion Review*. 29: 7–49.
2. Jiao, Z. and G. S. Was. 2011. "Impact of Localized Deformation On IASCC in Austenitic Stainless Steels." *J. Nucl. Mater.*, 408: 246–56.
3. Fukuya, K. 2013. "Current Understanding of Radiation-Induced Degradation in Light Water Reactor Structural Materials." *J. Nucl. Mater.*, 50(3): 213–54.
4. Fukuya, K., M. Nakano, K. Fujii, and T. Torimaru. 2004. "IASCC Susceptibility and Slow Tensile Properties of Highly-Irradiated 316 Stainless Steels." *J. Nucl. Sci. Technol.*, 41(6): 673–81.
5. Barnett, M. R., Z. Keshavarz, and M. D. Nave. 2005. "Microstructural Features of Rolled Mg-3Al-1Zn." *Metallurgical and Materials Transactions A*, 36(7): 1697–704.
6. Britton, T. B., J. Jiang, R. Clough, E. Tarleton, A. I. Kirkland, and A. J. Wilkinson. 2013. "Assessing the Precision of Strain Measurements Using Electron Backscatter Diffraction. Part 2: Experimental Demonstration." *Ultramicroscopy*, 135: 136–41.
7. Boehlert, C. J., S. C. Longanbach, M. Nowell, and S. Wright. 2008. "The Evolution of Grain-Boundary Cracking Evaluated through In Situ Tensile-Creep Testing of Udimet Alloy 188." *J. Mater. Res.*, 23(2).

8. Clair, A., M. Foucault, O. Calonne, Y. Lacroute, L. Markey, M. Salazar, V. Vignal, and E. Finot. "Strain Mapping Near a Triple Junction in Strained Ni-based Alloy Using EBSD and Biaxial Nanogauges." *Acta Materialia*, 59 (2011) 3116–23.
9. Massoud, J. P., P. Dubuisson, P. Scott, and V. K. Chamardine. 2005. *CIR II Program: Description of the Boris 6 and 7 Experiments in the BOR-60 Fast Breeder Reactor*. EPRI Report No. 1011787.
10. Scott, P. 2003. *Materials Reliability Program: A Review of the Cooperative Irradiation Assisted Stress Corrosion Cracking Research Program (MRP-98)*. EPRI Report No. 1002807.
11. Stephenson, K. J. and G. S. Was. 2014. "Crack Initiation Behavior of Neutron Irradiated Model and Commercial Stainless Steels in High Temperature Water." *J. Nucl. Mater.*, 444: 331–41.
12. Gussev, M. N., K. G. Field, and J. T. Busby, "Strain-induced phase transformation at the surface of an AISI-304 stainless steel irradiated to 4.4 dpa and deformed to 0.8% strain." *Journal of Nuclear Materials*, 446 (2014) 187–192.
13. Field, K. G., M. N. Gussev, and J. T. Busby, "Microstructural characterization of deformation localization at small strains in a neutron-irradiated 304 stainless steel." *Journal of Nuclear Materials*, 452 (2014) 500–508.
14. Was, G. S., Y. Ashida, K. J. Stephenson, A. Flick, and P. L. Andersen. *Identifying Mechanisms and Mitigation Strategies for Irradiation Assisted Stress Corrosion Cracking of Austenitic Steels in LWR Core Components*. EPRI Report No. 3002003105.
15. McMurtrey, M. D., G. S. Was, L. Patrick, and D. Farkas. 2011. "Relationship between Localized Strain and Irradiation Assisted Stress Corrosion Cracking in an Austenitic Alloy." *Mater Sci Eng.*, A528: 3730–40.